Biosensors and Bioelectronics 126 (2019) 734–742

Contents lists available at ScienceDirect

Biosensors and Bioelectronics

journal homepage: www.elsevier.com/locate/bios

Two-dimensional porphyrin-based covalent organic framework: A novel platform for sensitive epidermal growth factor receptor and living cancer cell detection

Xu Yan[a], Yingpan Song[b,1], Jiameng Liu[b,1], Nan Zhou[a,*], Chunlin Zhang[a], Linghao He[b], Zhihong Zhang[b,*], Zhongyi Liu[c,*]

[a] Department of Orthopedics, The First Affiliated Hospital of Zhengzhou University, No. 1, Jianshe East Road, Zhengzhou 450052, PR China
[b] Henan Provincial Key Laboratory of Surface and Interface Science, Zhengzhou University of Light Industry, No. 136, Science Avenue, Zhengzhou 450001, PR China
[c] College of Chemistry and Molecular Engineering, Zhengzhou University, Zhengzhou 450000, PR China

ARTICLE INFO

Keywords:
Porphyrin-based covalent organic framework
Electrochemical aptasensor
Detection of epidermal growth factor receptor
Living cancer cell detection

ABSTRACT

A porphyrin-based covalent organic framework (denoted as p-COF) was synthesized by a simple oil-bath method and exploited as a novel sensing layer for immobilizing epidermal growth factor receptor (EGFR)-targeting aptamer strands to detect trace EGFR and living michigan cancer foundation-7 (MCF-7) cells for the first time. p-COF presented a nanosheet-like structure, large cavities, rich nitrogen-bearing groups, high electrochemical activity, excellent bioaffinity, low toxicity, and good stability in aqueous solution; the microstructural features of this material enabled strong immobilization of the aptamer strands. Interactions between the aptamer strands and EGFR significantly changed the electrochemical signals of the modified electrode due to the formation of an aptamer-EGFR complex. The p-COF-based aptasensor exhibited an extremely low detection limit (LOD) of 5.64 fg·mL^{-1} obtained from differential pulse voltammetry and 7.54 fg·mL^{-1} originated from electrochemical impedance spectroscopy with a broad linear detection range of 0.05–100 pg·mL^{-1} of the EGFR concentration. When detecting living MCF-7 cells, the p-COF-based aptasensor showed an LOD of 61 cell·mL^{-1} with a linear detection range of 500 × 10^5 cell·mL^{-1}. The fabricated aptasensor exhibited high selectivity, good stability, reproducibility, acceptable recyclability, and favorable applicability in human serum samples. We believe that the developed p-COF-based aptasensor is a potential candidate for the sensitive detection of target cancer markers or living cells.

1. Introduction

Epidermal growth factor receptor (EGFR) is a transmembrane protein consisting of three major functional domains: an extracellular binding domain, a hydrophobic transmembrane domain, and an intracellular tyrosine kinase domain (Chu et al., 2015). Aberrant expression of EGFR (> 75.3 mg·L^{-1}) (Hasanzadeh et al., 2017) may be responsible for a number of cancers, such as lung, breast, prostate, bladder, colorectal, pancreatic, and ovarian cancers (Cohen, 2003). Therefore, in situ quantification of the EGFR expression level in the cell membrane and ligand binding kinetics and affinity are of great importance for cancer diagnosis and treatment (Zhang et al., 2015). Concurrently, the directly sensitive detection of cancer cells is also essential because of the urgent demand for rapid and highly effective methods for early diagnosing cancer. Nevertheless, since circulating tumor cells with very low concentrations of are present in the peripheral blood, it still remains challenging for detecting cancer cells with high specificity and sensitivity (Chinen et al., 2015). Therefore, it would be highly desirable to integrate two kinds of biosensors, which can simultaneously detect the cancer marker and cancer cells. Conventional methods for determination of EGFR as a cancer biomarker often include enzyme-linked immunosorbent assay (Pfeiffer et al., 1998), Western blot analysis (Thariat et al., 2012), and immuno-histochemistry (Hirsch et al., 2008). However, these approaches require sophisticated instrumentation, specially trained personnel, protein isolation, and clinically unrealistic expenses and time.

Aptamer, a single-stranded oligonucleotide sequence (RNAs or DNAs) artificially developed using systematic evolution of ligands via

* Corresponding authors.
E-mail addresses: fcczhoun@zzu.edu.cn (N. Zhou), mainzhh@163.com (Z. Zhang), liuzhongyi@zzu.edu.cn (Z. Liu).
[1] These authors contributed equally.

https://doi.org/10.1016/j.bios.2018.11.047
Received 9 September 2018; Received in revised form 10 November 2018; Accepted 28 November 2018
Available online 07 December 2018
0956-5663/

exponential enrichment technology (Chu et al., 2015), can sensitively and specifically conjugate with diverse kinds of targets, such as heavy metal ions (Tan et al., 2016), proteins (Yang et al., 2017a, 2017b), and hazardous small molecules (Nguyen et al., 2016). Aptamer sensors (aptasensors) outperform antibody-based assays due to their many advantages of low-cost, convenient synthesis, superior stability, site-specific labeling, site-specific immobilization, high sensitivity, reusability, and design flexibility (Meng et al., 2016). Howbeit, using aptamers for target detection often involves nucleic acid amplification strategies to amplify the target signal (Ma et al., 2016). Cancer markers, such as platelet-derived growth factor (Razmi et al., 2018), mucin 1 (Zhang et al., 2018a, 2018b), carcinoembryonic antigen and fetoprotein (Bao et al., 2018), vascular endothelial growth factor and prostate-specific antigen (Crulhas et al., 2017) were detected by their corresponding aptamers. Nevertheless the aptasensor have rarely been explored to quantitatively detect EGFR. For instance, the antibody-free fluorescence method for EGFR assay using aptamer as a probe was developed and exhibited a low detection limit (LOD) of 0.16 fM (Zhang et al., 2017a, 2017b). A electrochemical aptamer/antibody sandwich immunosensor for detecting EGFR was fabricated using a biotinylated anti-human EGFR aptemer immobilized on streptavidin-coated magnetic beads as a capture probe and a polyclonal anti-human EGFR antibody conjugated to citrate-coated gold nanoparticles (AuNPs) was used as a signaling probe, giving a high LOD of 50 pg mL^{-1} (Ilkhani et al., 2015). Gold nanoparticles (AuNPs) were modified by anti-EGFR antibody and EGFR aptamer to obtain multifunctional Apt-AuNP-Ab nanoconjugate immunoprobe, having a LOD of 0.1 ng mL^{-1} (Li et al., 2018a, 2018b). However, it clearly demonstrates that these methods often required cyclic signal amplification and labeling probe or targets, which complicates the treatment process and is time consuming. Therefore, sensitive, simple, fast, and low-cost methods are highly desirable for rapid quantification of EGFR. Among many detection approaches currently available, such as microfluidic immunosensor (Regiart et al., 2017), electrochemical method (Guo et al., 2017), and surface plasmon resonance (Zhang et al., 2015), electrochemical-based aptasensors should be exploited to sensitively detect EGFR because of their simplicity of operation, high affinity, relatively high selectivity, and sensitivity (Arya et al., 2018; Li et al., 2013). Among different electrochemical approaches, such as cyclic voltammetry (CV), differential pulse voltammetry (DPV), and electrochemical impedance spectroscopy (EIS), EIS often is employed to detect various analytes. Developing EIS aptasensors requires the immobilization of the aptamer on the transducer surface, providing a negatively charged interface that can result in impedance, especially when $[Fe(CN)_6]^{3-/4-}$ is used as redox agent (Zejli et al., 2018). Many nanomaterials, including carbon nanomaterials (graphene (Loan et al., 2018), carbon dots (Wang et al., 2017a, 2017b, 2017c), and carbon nanotubes (Magar et al., 2017)), magnetic nanoparticles (Zhang et al., 2018a, 2018b), polymers (Chen et al., 2017), quantum dots (Wang et al., 2017a, 2017b, 2017c), and porous organic frameworks (Yang et al., 2017a, 2017b), were used as effective signal amplification means to modify different electrodes (glassy carbon, gold and carbon paste electrodes), further being exploited as platforms to bind the probe molecules (antibodies or aptamers) and detect various analytes, as well as cancer cells (Hashkavayi et al., 2017). Consequently, it is pretty interesting to explore novel sensitive platforms, which exhibit good biocompatibility, high electrochemical activity, and strong bioaffinity toward biomolecules (Wang et al., 2017a, 2017b, 2017c), to fabricate the electrochemical biosensors for simultaneously detecting the cancer markers and cancer cells.

Recently, covalent organic frameworks (COFs) represent an emerging class of porous crystalline polymers with structural periodicity and inherent porosity. COFs have attracted considerable research attention and show promising applications in gas storage, chemosensors, heterogeneous catalysis, capacitors, batteries, drug delivery, energy conversion, and storage (Díaz and Corma, 2016) on account of their large surface area, low density, biodegradability, nontoxicity, and high thermal stability. Several COF-based sensing strategies have been designed to detect various important targets, such as organic molecules (Geng et al., 2018), trace water in organic solvents (Qian et al., 2017), and heavy metal ions (Xiong et al., 2017). Usually, COFs were exploited as the fluorescence biosensors rather than electrochemical ones (Ding et al., 2016). Fluorescent dye-labeled DNA probes, and the fluorescence of the dye was quenched via fluorescence resonance energy transfer, giving excellent selectivity and high sensitivity (Peng et al., 2017). Similarly, as reported by Li et al., COF films can be functionalized with different groups and endowed with different charges, thereby allowing them to electrostatically interact with other molecules and strengthen the electrochemical activity of the reaction system. Fang et al. synthesized imine-linked COF films onto amino functionalized silicon wafers and obtained positively charged hybrid films due to the presence of amino groups (-NH_2) (Wang et al., 2014). However, COF-based electrochemical sensing strategies are highly limited by several limitations, including high background noise, low sensitivity, and lack of a specific recognition group. Few reports on the applications of COFs in biosensing fields, especially for the detection of cancer markers, are yet available. To the best of our knowledge, no report on the development of COFs-based electrochemical aptasensors has yet been published.

Herein, we designed and developed a novel aptasensor based on porphyrin-based COF (p-COF) that can selectively and sensitively bind with EGFR and detect human breast carcinoma MCF-7 cells. Compared with routine aptasensors, the fabricated p-COF-based aptasensor exhibits outstanding sensing performances toward various analytes, including simultaneously detecting EGFR and living cancer cells, label-free fabrication and simple detection procedure, and ultra-sensitive and selective detection. The remarkable sensing performance of p-COF for EGFR and living cancer cells can be mainly attributed to the following factors. (i) Two-dimensional nanosheet structure of p-COF can produce much more binding sites for aptamer strands or biomolecules (Suzuki et al., 2015); (ii) Highly conjugated structure of p-COF not only can enhance the binding force between biomolecules and p-COF but also can improve the electrochemical activity in comparison with other normal COFs; (iii) Large pore channel of p-COF facilitates the aptamer strands to immobilize within the interior of p-COF, which can increase the adsorbed amount of the probe and further enhance the detection sensitivity toward analytes (Wan et al., 2011). As expected, the fabricated p-COF-based aptasensor showed excellent sensing performance toward EGFR and living MCF-7 cells, including high sensitivity, good selectivity, and acceptable stability.

2. Experimental section

The methods used for pretreatment of the bare Au electrode (AE) and preparation of phosphate buffered saline (PBS, pH 7.4), aptamer, EGFR, and human serum solutions, cell culture, in vitro cytotoxicity test, intracellular uptake study, and basic characterizations are provided in **S1**(the Supplementary Information (SI)).

2.1. Synthesis of p-COF nanosheets

p-COF was synthesized according to the method proposed by Wan et al.(Wan et al., 2011) with some modifications. Supramolecular p-COF was synthesized by a simple and facile oil-bath approach using 5,10,15,20-tetrakis(4-aminophenyl) porphyrin (TAPP) and terephthaldehyde as monomers. Amino groups in TAPP and aldehyde groups (-CHO) in terephthaldehyde can react with each other via nucleophilic addition-elimination to generate imine groups (C=N-) (Scheme 1). In a typical synthesis procedure, 6 mg of terephthaldehyde was dissolved in 6 mL of DMSO. Then, 10 mg of TAPP was added to this mixture, and the reaction system was placed in an oil bath at 90 °C for 2 d. The product was washed repeatedly with tetrahydrofuran and ethanol and then dried at 60 °C in an oven to yield p-COF.

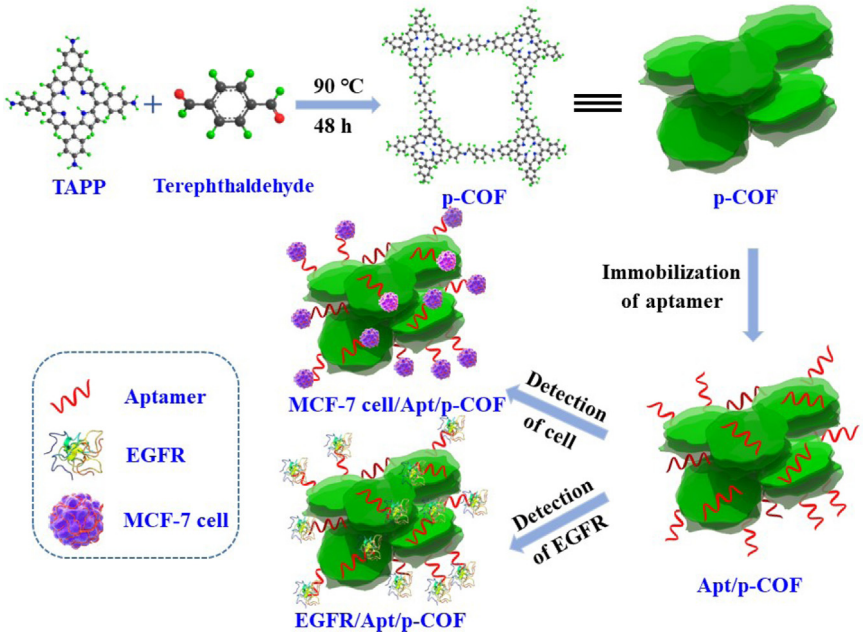

Scheme 1. Schematic diagram of the p-COF-based aptasensor for detecting EGFR or MCF-7 cells, including (i) preparation of p-COF, (ii) immobilization of the aptamer strands, and (iii) detection of EGFR or MCF-7 cells.

2.2. Fabrication of the p-COF-based aptasensor

p-COF was first dispersed in ultrapure water to obtain a homogeneous suspension with a concentration of 1.0 mg mL^{-1}. Approximately 10.0 μL of the p-COF dispersion was then dropped onto the surface of the pre-treated bare AE. The p-COF-modified AE was rinsed several times with ultrapure water and dried under a N_2 stream. The p-COF-based aptasensor benefits from the C=N- and secondary -NH_2 groups, as well as the macromolecular structure, of p-COF. It possesses a π-conjugated network, and its electrons are expected to migrate quickly into the p-COF layers.

Subsequently, the p-COF-modified AE was immersed first in the aptamer solution for 2 h at 4 °C and then in EGFR solutions of different concentrations for 2 h to enable detection of the target EGFR.

2.3. Electrochemical measurements and EIS spectra

Cyclic voltammetry (CV), differential pulse voltammetry (DPV), and electrochemical impedance spectroscopy (EIS) were conducted on the CHI 660E electrochemical station with a traditional three-electrode system. The bare AE or modified AE, Ag/AgCl and Pt wire were used as working electrode, reference electrode and counter electrode, respectively. CV curves were measured in the mixture of 5.0 mM $K_3[Fe(CN)_6]/K_4[Fe(CN)_6]$ (1:1) as a redox probe dissolved in 0.10 M PBS at potentials ranging from −0.2–0.8 V vs. Ag/AgCl (saturated KCl) at the scan rate of 100 mV $^{-1}$. DPV measurements were performed with the following parameters: impulse amplitude of 50 mV, potential scan from −0.2–0.8 V, and step potential of 4 mV. EIS spectra were recorded at a bias potential of 0.22 V vs. Ag/AgCl (saturated KCl) and 5 mV amplitude in the frequency ranging from 0.01 Hz to 100 kHz. The EIS data were analyzed using Zview2 software, of which EIS spectra were simulated using an equivalent circuit consisted of solution resistance (R_s), charge-transfer resistance (R_{ct}), constant-phase element (CPE), and Warburg impedance (W_o) (the inset in Fig. S1). Each measurement was repeated at least three times.

In case of electrochemical experiments of the p-COF-based aptasensors for detecting MCF-7 cells, p-COF-modified AE was acted as the working electrode and placed near the live cells, and the EIS responses were recorded by CHI 660E.

3. Results and discussion

3.1. Sensor design

p-COF was prepared using TAPP and terephthaldehyde as ligands and DMSO as a solvent in an oil bath and then used as the sensing layer for immobilizing label-free EGFR-targeting aptamer stands (Apt) via electrostatic interactions between the positively charged imine onium salt in p-COF and the negatively charged aptamer base pairs, as well as the π-π stacking effect and hydrogen bonding (Li et al., 2017; Peng et al., 2017). As p-COF exhibits high charge carrier mobility, large pore cavities, and good electrochemical activity after functionalization (Zhao et al., 2018), the aptamer strands can not only adsorb onto the p-COF surface but also penetrate the interior of the porous framework. Large amounts of immobilized aptamer strands on the modified electrode surface block the charge transfer process between the electrode and electrolyte solution, leading to a decrease in electrochemical signals. When Apt/p-COF is exposed to EGFR solution or living MCF-7 cells, interaction with the aptamer strands occurs via biorecognition between these strands and the EGFR or cells. This interaction considerably lowers the access of the redox probe ($[Fe(CN)_6]^{3-/4-}$) to the surface of the modified electrode. The decrease in electrochemical responses is then determined by electrochemical techniques (Scheme 1).

3.2. Crystal structure and chemical components of p-COF

The chemical structure and crystal components of p-COF were analyzed by FT-IR, XPS, and XRD. As shown in Fig. S2a, TAPP (curve i) presents no obvious typical characteristic absorption bands. By contrast, p-COF exhibits a characteristic absorption band at 1659 cm^{-1} (curve ii), which corresponds to the C=N- stretching of imine groups and confirms the formation of an imine bond after the condensation reaction of -NH_2 in TAPP and -CHO in terephthaldehyde. The intense and broad band centered at 3432 cm^{-1} is ascribed to the O-H stretching mode of crystalline water and physiosorbed water condensed inside the COF cavities, while the intense doublet at 629 cm^{-1} is attributed to the -OH groups of H_2O molecules. The XRD patterns of TAPP and p-COF (Fig. S2b) show three typical diffraction peaks at 2θ = 26°, 33°, and 52°. The peak at 26° is assigned to the (002) lattice plane of graphitic

carbon, which indicates that the π-conjugated structure is retained after the reaction of TAPP with terephthaldehyde. The chemical structure of p-COF was further confirmed by ^{13}C NMR, as displayed by Fig. S3, of which solid state ^{13}C NMR is ascribed to δ = 158.85 (C=N), 149.82, 139.46, 130.21, and 119.49 ppm. These results demonstrate that the C=N bond is formed after the condensation reaction of -NH_2 in TAPP and -CHO in terephthaldehyde and prove the successful synthesis of p-COF.

To evaluate the chemical components of the prepared p-COF, XPS analysis was performed. The XPS survey spectra of TAPP and p-COF are composed of the spectra of C 1 *s*, N 1 *s*, and O 1 *s* (Fig. S4). As shown in Fig. S5a, the core-level C 1 s XPS spectrum of TAPP could be separated into three main parts; here, peaks located at 283.7, 284.3, and 285.0 eV are ascribed to C=C, C-C, and C-N, respectively. Three other weak peaks at 286.3 (C-O), 288.2 (N-C=O), and 290.7 eV (π-π *) indicate that TAPP possesses a π-conjugated structure. Trace amounts of oxygen could be attributed to oxygen contamination during the test process. The N 1 *s* core-level XPS spectrum of TAPP (Fig. S5b) could be fitted into three main parts; here, the peaks at 397.4, 399.1, and 399.9 eV, along with another weak peak at 402.2 eV, correspond to atomic β-N, pyridinic N, pyrrolic N, and pyridinic -(N^+-O^-), respectively (Vinayan et al., 2012). For p-COF (Fig. S6a1), aside from three main peaks at 284.7 (C-C), 285.8 (C-N), and 288.3 eV (N-C=O), an additional peak at 291.5 eV is obtained, which is assigned to π-π^* binding. This additional peak indicates the successful extension of the planar π-electron conjugated system contained in p-COF, which endows the material with high charge carrier mobility and facilitates the charge transfer process (Wan et al., 2011). In the case of p-COF (Fig. S6b1), only two peaks at 397.9 (atomic β-N) and 399.9 eV (pyrrolic N) are observed. Here, the pyrrolic N contributes to the electron density to the π-conjugated system with a pair of p-electrons in the p-COF layers. The O 1 *s* core-level XPS spectrum of p-COF (Fig. S6c1) shows two peaks at 531.5 and 532.5 eV, which are due to C=O and C-O, respectively, and demonstrates that oxygen is introduced by terephthaldehyde, thus confirming the chemical reaction between TAPP and terephthaldehyde. After the aptamer strands immobilization, an additional peak at 286.4 eV in the C 1 *s* core-level XPS spectrum (Fig. S6a2), O=C, was observed, which is caused by the presence of the oligonucleotide molecules. In case of N 1 *s* core-level spectrum (Fig. S6b2), two additional peaks are obtained at 400.2, and 402.3 eV, which are assigned to N-C=O and N-O_x groups, respectively. And the relative intensity of C=O containing in the O 1 *s* core-level XPS spectrum increases (Fig. S6c2), which also can be explained by the immobilization of aptamer strands. In addition, a weak signal of P 2*p* core level XPS spectrum shows two peaks at ~133.5 and ~134.4 eV, which are assigned to P $2p_{3/2}$ and P $2p_{1/2}$, respectively (Fig. S7) can prove the above discussion. Moreover, the permanent porosity of p-COF was determined by the N_2 adsorption-desorption isotherms (Fig. S8a). It shows a type-I isotherm with a Brunauer − Emmett − Teller (BET) surface area of 117.2 $m^2 \cdot g^{-1}$ and a total pore volume of 0.23 $cm^3 \cdot g^{-1}$. It also reveals a narrow distribution centered at around 2 nm (Fig. S8b), indicating of microporous structure of p-COF. The relatively large specific surface area and porous structure are benefit for the aptamer strands not only anchoring onto the p-COF surface but also penetrating into the framework via physical interactions or hydrophobicity.

3.3. Surface morphology of the p-COF

The surface morphology and microstructure of the TAPP and p-COF nanosheets were characterized by FE-SEM and HR-TEM. As shown in Fig. S9, TAPP shows a platelet structure with an average size of 800 nm - 1.5 μm. Most of the TAPP platelets aggregate into large blocks owing to strong molecular forces in the reaction system. SEM images of p-COF display a sheet-like structure with an average size of approximately 1 μm (Figs. 1a and b); most of the nanosheets aggregate into large blocks due to interlayer π–π stacking interactions (Gao et al., 2018). These features indicate the formation of p-COF after the reaction of TAPP with terephthaldehyde in the oil bath. The HRTEM of p-COF (Figs. 1c–e) exhibits a two-dimensional (2D) nanostructure with several thin monolayers stacked to form a large block. The large block exhibits clear and regular edges and pore channels within the sheet layers. The diameter of the pore channels is estimated from Fig. 1e to be about 2.06 nm; large pore cavities in p-COF not only enhance electron transfer along the organic framework (Wan et al., 2011) but also facilitate the anchoring of aptamer strands. They also endow the aptamer strands with the ability to both adsorb onto the p-COF surface and penetrate into the p-COF interior (Zhang et al., 2017a, 2017b). The AFM image of p-COF displays that the thickness of the nanosheets is about 6.0–7.0 nm (Fig. S10), demonstrating a two-dementional characteristic of the synthesized p-COF.

3.4. Electrochemical performance of the p-COF-based aptasensor toward EGFR

Electrochemical techniques, including CV, DPV, and EIS, were applied to investigate the electrochemical response of the p-COF-modified electrode, monitor both the construction and sensing process of the proposed aptasensor, and provide significant information about the whole fabrication procedure of the working electrode. The CV curves display a pair of typically well-defined reversible redox peaks with a peak-to-peak separation (ΔE_p) of 228.0 mV for the bare AE (Fig. 2**a**). For the p-COF-modified AE (p-COF/AE), ΔE_p increases to 234.2 mV with decreasing redox peak currents. This result indicates that p-COF exhibits relatively poor electrochemical activity, resulting in a decrease in current density. When EGFR-targeting aptamer strands are immobilized onto the p-COF/AE surface (denoted as Apt/p-COF/AE), ΔE_p strongly increases to 289.6 mV and the redox peak current shows successive decreases, thus suggesting the strong blocking effect of the EGFR-targeting aptamer on p-COF/AE (Arya et al., 2018). When the prepared Apt/p-COF/AE is immersed into EGFR solution to detect EGFR (EGFR/Apt/p-COF/AE), ΔE_p further increases to 365.6 mV and the redox peak current decreases. This result proves that declines in the conductivity and electrochemical activity of EGFR/Apt/p-COF/AE are due to the blocking effect of EGFR (Li et al., 2013). Additionally, the EIS response of p-COF without aptamer for detecting EGFR was performed, along with the measurements for the adsorption of other interferents (BSA, CEA, HER2, IgG, MUC1, PSA, and VEGF), as displayed in Fig. S11. The results displayed that the unconspicuous signal was obtained after EGFR immobilization over the p-COF/AE, while the same observation was found for other interferents. It means that the p-COF platform without EGFR-targeted aptamer immobilization could not directly applied to detect analyte owing to the non-specific interaction between the analyte molecules and p-COF.

The electrochemical results described above were confirmed by DPV measurements. The DPV curves in Fig. S12 reveal that the peak current (I_p) of the bare AE is −72.1 μA. After modification with p-COF, the I_p of the electrode decreases to −67.9 μA. The absolute value of I_p clearly decreases, which means the electrochemical activity of p-COF/AE is slightly lower than that of the bare AE. The I_p Apt/p-COF/AE and EGFR/Apt/p-COF/AE decrease to −63.2 and −56.4 μA, respectively, which confirms the previously observed decrease in electrochemical activity after immobilization of the aptamer and detection of EGFR.

The CV and DPV results are consistent with the Nyquist plots obtained for the complete process of EGFR detection using the p-COF-based aptasensor. As shown in Fig. 2b, the R_{ct} of the AEs at different fabrication stages of bare AE, p-COF/AE, Apt/p-COF/AE, and EGFR/Apt/p-COF/AE are 0.05, 0.25, 0.37, and 0.62 kohm, respectively. These values show that the electrochemical activity of the electrode continually decreases after modification with p-COF, EGFR-targeting aptamer immobilization, and EGFR detection. Next, the variation in R_{ct} (ΔR_{ct}) for each step is calculated, and the ΔR_{ct} obtained after p-COF modification ($R_{ct,\ material} - R_{ct,\ AE}$) is 0.20 kohm. Compared with those

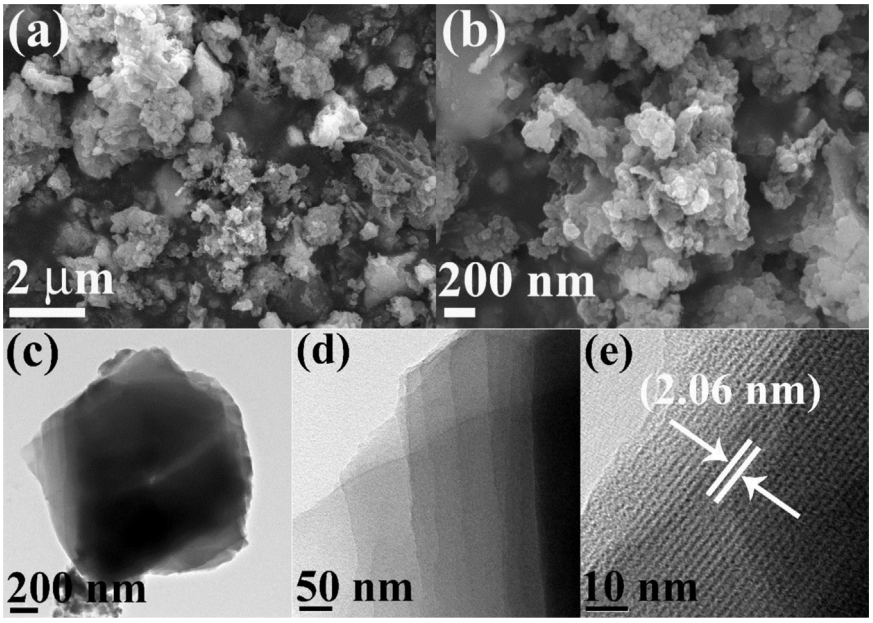

Fig. 1. (a, b) FE-SEM and (c, d, e) HR-TEM images of p-COF nanosheets.

of metal oxides, such as Fe_3O_4 @mC (Song et al., 2017), and MOFs (He et al., 2017), the smaller R_{ct} of p-COF reveals its relatively good electrochemical activity. Therefore, p-COF can be employed as the sensing layer for aptamer strand immobilization. Aptamer strand anchoring reveals a small ΔR_{ct} ($R_{ct,\ Apt} - R_{ct,\ material}$) of only 0.12 kohm, but EGFR detection yields a large ΔR_{ct} ($R_{ct,\ EGFR} - R_{ct,\ Apt}$) of (0.25 kohm). Immobilization of EGFR-targeting aptamer strands onto p-COF/AE (Apt/p-COF/AE) restrains the access of the electrolyte to the modified electrode surface due to the repulsion between negatively charged phosphate groups in the aptamer strands and the redox probe, $[Fe(CN)_6]^{3-/4-}$, (Top et al., 2016) further resulting in low charge transfer efficiency and increases in R_{ct}. When Apt/p-COF/AE is used to detect EGFR, the EGFR aptamer can change its conformation to specifically bind with EGFR, thereby generating biorecognition interactions between the aptamer and EGFR to form an aptamer-EGFR complex. This complex blocks charge transfers between the electrode and the electrolyte solution (Li et al., 2013). The large ΔR_{ct} for EGFR detection suggests that the adsorption interaction between the components of the aptamer-EGFR complex is enough strong to stably retain over the p-COF-based aptasensor, leading to enhancement of the detection efficiency of the

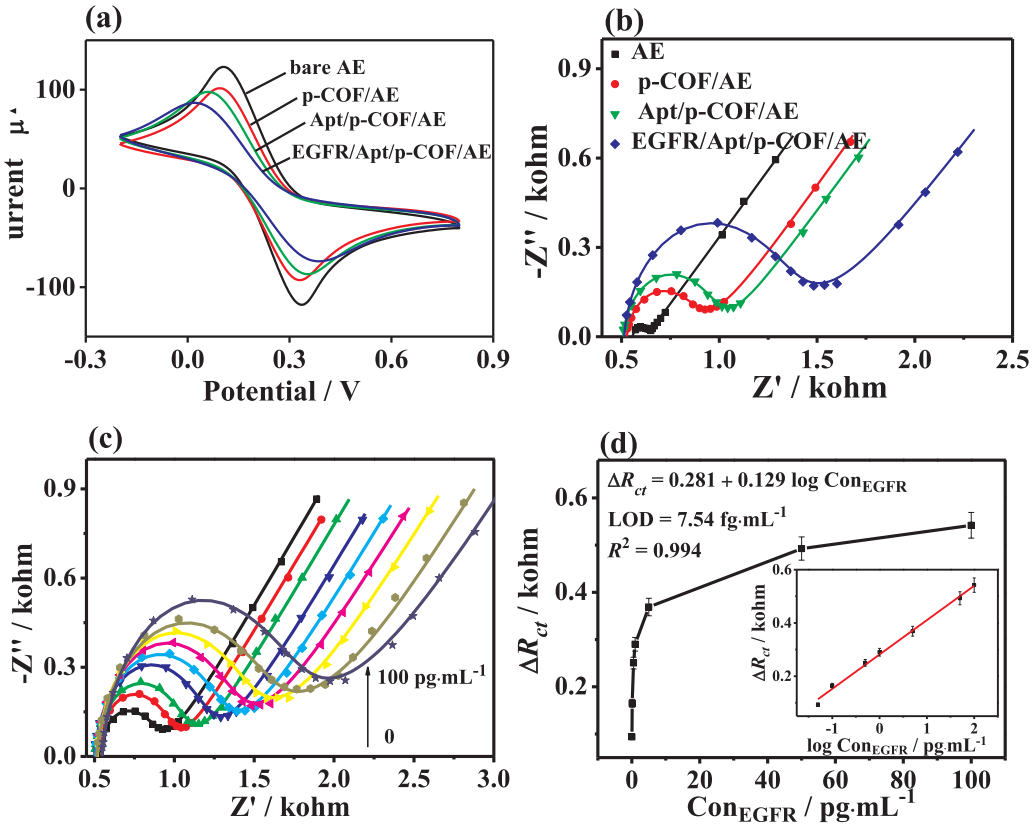

Fig. 2. (a) CV curves and (b) EIS Nyquist plots of p-COF-based aptasenosr for detection of EGFR in 5 mM $[Fe(CN)_6]^{3-/4-}$ containing 0.1 M KCl, including (i) AE, (ii) P-COF/AE, (iii) Apt/P-COF/AE, and (iv) EGFR/Apt/p-COF/AE. (c) EIS responses of the Apt/p-COF/AE with different EGFR concentrations (0, 0.05, 0.1, 0.5, 1, 5, 50, and 100 pg·mL^{-1}). (d) Dependence of ΔR_{ct} on the concentration of EGFR. The linear parts of the calibration curves are shown in the inset of (c).

electrode toward EGFR.

3.5. Sensitivity of the p-COF-based aptasensor toward EGFR

To evaluate the analytical performance of the proposed aptasensor, we incubated Apt/p-COF/AE with different concentrations of EGFR and subsequently measured the resulting signals by EIS in $[Fe(CN)_6]^{3-/4-}$ and 0.1 M PBS, as illustrated in Fig. 2c. The R_{ct} values substantially increase with increasing EGFR concentration over the range of 0.05–100 pg·mL^{-1} due to the efficient biorecognition interaction between EGFR and the aptasensor (Arya et al., 2018). Thereafter, the R_{ct} values slowly increase due to the saturated interaction between the aptamer strands and EGFR (Arya et al., 2018). When the ΔR_{ct} of the aptasensor before and after EGFR detection ($R_{ct,\ EGFR} - R_{ct,\ Apt}$) is referred to as the determined signal (Fig. 2d), ΔR_{ct} is highly proportional to the logarithm of the EGFR concentration (log Con_{EGFR}); the resulting linear regression equation is ΔR_{ct} (kohm) = 0.281 + 0.129 log Con_{EGFR} (pg·mL^{-1}) with a correlation coefficient (R^2) of 0.994. According to the Langmuir adsorption equation (Pauchard et al., 2014), the LOD is calculated to be low (7.54 fg·mL^{-1}) at a signal-to-noise (s/n) ratio of 3, together with the relative standard deviation (RSD) of 1.28%. Additionally, the LOD for the EGFR detection was also determined by using DPV method and is evaluated to be 5.64 fg·mL^{-1} (Fig. S13), which is consistent with EIS result.

Compared with other nanomaterial-based EGFR aptasensors (Table 1), the proposed p-COF-based aptasensor exhibits superior sensing performance and provides a broad linear range of EGFR and low LOD. p-COF exhibits a nanosheet-like highly π-conjugated structure and large pore channels (2.06 nm), both of which allow immobilization of large amounts of aptamer strands via hydrogen bonding, π–π stacking, and electrostatic interactions (Li et al., 2017; Peng et al., 2017; Shi et al., 2017). The unique chemical structure of this framework can stabilize the complex formed between the aptamer strands and EGFR, resulting in sensitive detection of EGFR (Johari-Ahar et al., 2018) and cancer cells. The high electrochemical activity of p-COF can also enhance the electrochemical activity of the resulting electrode and amplify its output signal, unlike other polymeric (Li et al., 2018a, 2018b) or metal oxide (Emami et al., 2014) electrode materials. These features endow the p-COF-based aptasensor with exceptional sensing performance even when detecting trace analytes.

3.6. Selectivity, stability, reproducibility, and recyclability of the p-COF-based aptasensor

The selectivity of an electrochemical aptasensor is an important parameter to consider in its performance. Herein, interferences, including CEA, PSA, MUC1, HER2, VEGF, IgG, PDGF-BB, and BSA, which often coexist with EGFR in human serum, were detected under the same conditions by EIS using the p-COF-based aptasensor. As displayed in Fig. 3a the change in ΔR_{ct} induced by addition of 0.1 ng mL^{-1} interferences, which is 1000-fold of the concentration of the EGFR solution (0.1 pg mL^{-1}) is negligible; by contrast, exposure of the aptasensor to the EGFR solution leads to an obvious ΔR_{ct} of 0.198 kohm. When EGFR is mixed with these interferences, a clear response of the ΔR_{ct} is also observed (0.202 kohm), which is comparable with that of the EGFR solution. This result demonstrates the high selectivity of the electrochemical aptasensor for EGFR detection over other proteins because of the specific biorecognition between EGFR and the EGFR-targeting aptamer.

To determine the stability of the p-COF-based aptasensor (Fig. 3b), its responses after daily exposure to 0.1 ng·mL^{-1} EGFR and storage in the dry state at 4 °C were detected. The ΔR_{ct} of the aptasensor is about 101.1% of its original response after over 10 d of storage, which means it possesses good stability. In addition, five p-COF-modified AEs were prepared independently and used to determine EGFR (0.1 pg mL^{-1}) under identical conditions; this experiment revealed acceptable reproducibility with an RSD of 2.29% (Fig. 3c). Such a result indicates that the aptasensor gives good reproducibility and precision. The recyclability of the fabricated aptasensor was evaluated by immersing the EGFR-bound nanocomposite electrode into 0.1 M KOH at room temperature for 10 min, followed by rinsing with a large amount of ultrapure water. Thereafter, the treated electrode was immersed into EGFR solution (0.05 pg·mL^{-1}). Fig. 3d shows no substantial change in the ΔR_{ct} of the aptasensor over eight regeneration runs, thus suggesting that it can be successfully recycled.

3.7. Aptasensor application

We investigated the practical use of the electrochemical aptasensor for EGFR detection in human serum samples by detecting EGFR in human serum samples obtained from healthy persons. Different EGFR concentrations were spiked into the treated human serum samples, and the presence of EGFR was detected and analyzed using the developed p-COF-based aptasensor via the electrochemical sensing method described above. Results were obtained and plotted to a standard curve (the inset of Fig. 2d). As shown in Table S1, the recovery of the proposed aptasensor ranges from 96.2% to 103.2% with all RSDs below 4%. The results suggest that the new detection strategy developed in this work exhibits high reproducibility, accuracy, and feasibility for rapidly detecting EGFR in human serum.

3.8. Biocompatibility of p-COF with living MCF-7 cells and in vitro cell uptake of the p-COF nanosheets

The cell viability of p-COF was evaluated by incubating the material with MCF-7 cell lines in vitro. As displayed in Fig. S14a, a minute difference in the cytotoxicity of p-COF was observed after 24 h. 90% of the MCF-7 cells remained alive even at p-COF dosages as high as 200 μg·mL^{-1}. This result indicates that the p-COF nanosheets are biocompatible with MCF-7 cells and could be attributed to the nontoxicity of the framework, which only contains C, N, and O. Therefore, the p-COF-based aptasensor can be used to directly detect living MCF-7 cells

Table 1
Comparison with other reported techniques for EGFR detection.

Materials	Detection method	Detection range (pg·mL^{-1})	LOD (pg·mL^{-1})	Refs.
MIP-Ab_{EGFR}-Cd (II)@LP-Ab_{VEGF}-Cu(II)@LP	potentiometric striping analysis	0.05–50,000	0.01	(Johari-Ahar et al., 2018)
Pb_{NC}@BSA	square wave anodic stripping voltammetry	400–35,000	8	(Mousavi et al., 2016)
CMK3-poly(AC-*co*-MDHLA)	amperometry	10–50,000	3.03	(Regiart et al., 2017)
Fe_3O_4/N-trimethyl chitosan/Au	DPV	0–1000	0.05	(Omidfar et al., 2015)
ferrocene-labeled peptide ligand	DPV	0.1–10,000	0.037	(Li et al., 2013)
AuNPs-Protein G	Impedance	1–1,000,000	0.34	(Elshafey et al., 2013)
Anti-EGFRab/DTSP/Au	CV	1–100,000	1	(Vasudev et al., 2013)
primer 1 + primer 2 + EGFR	fluorescence	0.17–170,000	0.0272	(Zhang et al., 2017a, 2017b)
p-COF	EIS	0.05–100	7.54×10^{-3}	**This work**
	DPV	0.05–100	5.64×10^{-3}	

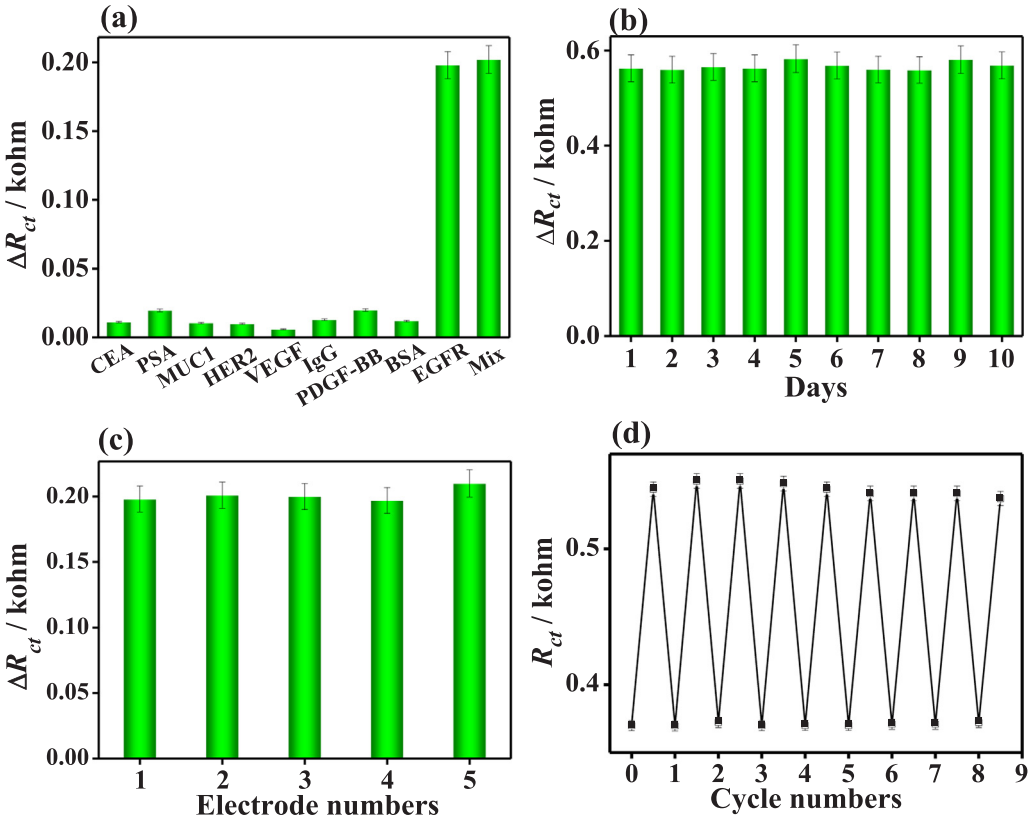

Fig. 3. (a) ΔR_{ct} values of p-COF-based electrochemical aptasensor by separately adding the interferences (CEA, PSA, MUC1, HER2, VEGF, IgG, PDGF-BB, and BSA with the concentration of 0.1 ng·mL^{-1}), EGFR (0.1 pg·mL^{-1}), and their mixture. (b) Stability of the p-COF-based electrochemical aptasensor for detecting EGFR (0.1 ng·mL^{-1}) within 10 days. (c) Reproducibility of the p-COF-based aptasensor for detecting EGFR with the concentration of 0.1 pg·mL^{-1}. (d) Regenerability of the p-COF-based aptasensor for detecting EGFR with the concentration of 0.05 pg·mL^{-1}.

expressing EGFR during their cellular metabolism.

The cell uptake of p-COF was measured by incubation of the material with MCF-7 cells followed by confocal laser scanning microscopy. The results are shown in Fig. S14b. Black dots at the exterior of the MCF-7 cells in bright-field mode reflect p-COF. After excitation of these cells by a 400 nm laser, weak green fluorescence, which is attributed to the fluorescent property of p-COF, is observed. The merged photo confirms that p-COF is preferentially accumulated in cancer cells and directly generates fluorescence without requiring the use of other dyes. This phenomenon indicates the feasibility of using p-COF for live cell imaging and targeted drug delivery and release.

3.9. Electrochemical performance of the p-COF-based aptasensor toward MCF-7 cells

The p-COF-based aptasensor was employed to detect living MCF-7 cells by EIS, as illustrated in Fig. 4a. Modification of AE with p-COF, immobilization of aptamer strands, and detection of MCF-7 cells caused successive increases in the R_{ct} of the electrode, which means the biorecognition interaction between the aptamer strands and MCF-7 successfully takes place. Consequently, the fabricated p-COF-based aptasensor can be exploited to directly detect cancer cells via the electrochemical technique.

The p-COF-based aptasensor was used to detect normal L929 cells by EIS to evaluate its selectivity, as shown in Fig. 4b. No substantial change in the EIS response was observed after the modified electrode was incubated in the L929 cell solution (500 cells·mL^{-1}) for 1 h. This observation confirms that the constructed p-COF-based aptasensor can not only be employed in the determination of the cancer marker but also be exploited in clinical analysis.

MCF-7 cells were centrifuged at 2000 rpm for 3 min to separate the culture medium, collected, and then carefully dispersed into PBS to obtain different cell concentrations (5 ×10^2, 1 ×10^3, 5 ×10^3, 1 ×10^4, 5 ×10^4, 1 ×10^5 cell mL^{-1}). The modified electrode was incubated with the cell solutions at 37 °C for 60 min, followed by fully rinsing to clean out the nonspecifically bound cells. EIS was then employed to study the electrochemical behavior of the aptasensor and characterize its detection efficiency. As shown in Fig. 4c, the R_{ct} values substantially increase with increasing MCF-7 cell concentration over the range of 5 × 10^2-1 × 10^5 cell·mL^{-1} due to the efficient biorecognition interaction between the aptamers immobilized on the aptasensor and the EGFR expressed by the MCF-7 cells. The R_{ct} values then slowly increase due to saturation of the interaction between the aptasensor and cells. When the ΔR_{ct} of the aptasensor before and after MCF-7 cell detection ($R_{ct,\ \text{MCF-7}} - R_{ct,\ \text{Apt}}$) is referred to as the determined signal (Fig. 4d), the ΔR_{ct} is proportional to the logarithm of the MCF-7 cell concentration (log $\text{Con}_{\text{MCF-7}}$). The linear regression equation is ΔR_{ct} (kohm) = −1.197 + 0.49 log $\text{Con}_{\text{MCF-7}}$ (cell·mL^{-1}) with an R^2 of 0.993. The LOD is calculated to be 61 cells·mL^{-1} at an S/N ratio of 3, and the RSD is 1.37%. As a result, the LOD was estimated to be 61 cells mL^{-1}. It reveals that the p-COF-based aptasensor shows superiority over recently reported MCF-7 sensors in analytical performance (Table S2). This excellent sensing performance of the p-COF-based aptasensor is mainly ascribed to the large specific surface area, strong aptamer binding interaction, and high electrochemical activity. Additionally, Fig. S15 shows the EIS responses of the Apt/p-COF/AE for detecting L929 cells with different concentrations. It shows that the R_{ct} values increase at the relatively low L929 cell concentrations (5 ×10^2 and 1 ×10^3 cells·mL^{-1}). However, when the cell concentrations further increase to 5 × 10^3 and 1 × 10^4 cells mL^{-1}, the EIS signal are up to an equilibrium. It is mainly owning to that the AS1411 aptamer can not recognize the normal L929 cells. Moreover, excellent reproducibility and stability were also obtained using the same p-COF-based aptasensor for five repeated tests with different cell concentrations (Fig. S16).

4. Conclusions

In summary, a novel electrochemical p-COF-based aptasensor was fabricated for the ultra-sensitive detection of EGFR and living MCF-7 cells. Results indicated that p-COF possesses a 2D highly π-conjugated

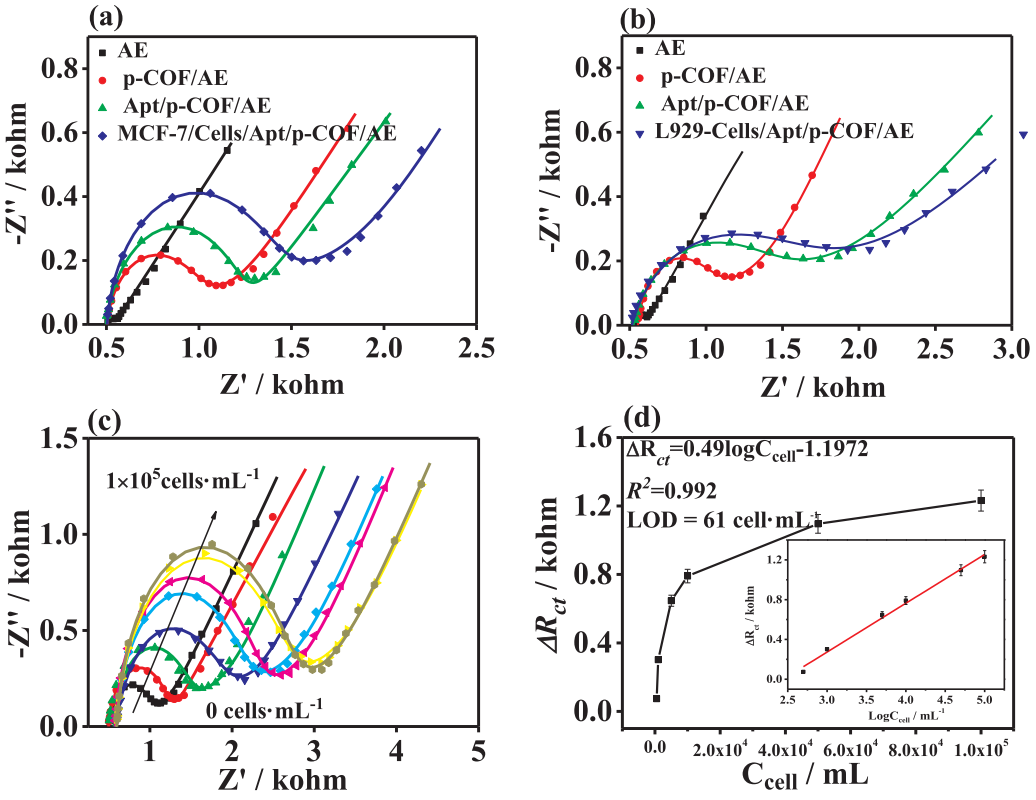

Fig. 4. EIS Nyquist plots of p-COF modified AEs for detection of (a) MCF-7 and (b) L929 cells in 0.1 M PBS (pH 7.4) containing 5.0 mM $[Fe(CN)_6]^{3-/4-}$ redox. (c) EIS responses of the Apt/p-COF/AE with different MCF-7 cell concentrations (0, 5 ×10^2, 1 ×10^3, 5 ×10^3, 1 ×10^4, 5 ×10^4, 1 ×10^5 cells mL^{-1}). (d) Dependence of ΔR_{ct} on the concentration of MCF-7 cell. The linear parts of the calibration curves are shown in the inset of (c).

nanostructure, large pore cavities (2.06 nm), excellent electrochemical activity, good biocompatibility, and low toxicity. The microstructural features of the framework facilitate immobilization of aptamer strands onto the modified electrode surface through electrostatic, hydrogen bonding, and π-π stacking interactions. When exposed to EGFR or MCF-7 cells, the electrochemical response of Apt/p-COF/AE decreased because of the specific biorecognition interaction between the aptamer strands and EGFR or cells. Electrochemical results revealed that the p-COF-based aptasensor exhibits low LODs of 5.64 and 7.54 fg·mL^{-1} for EGFR by using DPV and EIS and 61 cells·mL^{-1} for direct detection of living MCF-7 cells. The fabricated aptasensor also demonstrated excellent selectivity toward other protein interferences, good stability, reproducibility, acceptable recyclability, and applicability in human serum samples. Therefore, the proposed aptasensor may provide a new biosensing platform for the rapid and sensitive detection of trace EGFR and living cancer cells. The results of this work present important insights into novel approaches for disease diagnosis and subsequent therapy monitoring.

Acknowledgements

This work was supported by Programs for the National Natural Science Foundation of China (NSFC: Account Nos. 81601082, 81371363, 81771329 and U1604127) and Innovative Technology Team of Henan Province, China (CXTD2014042).

Appendix A. Supplementary material

Supplementary data associated with this article can be found in the online version at doi:10.1016/j.bios.2018.11.047.

References

Arya, S.K., Zhurauski, P., Jolly, P., Batistuti, M.R., Mulato, M., Estrela, P., 2018. Biosens. Bioelectron. 102, 106–112.
Bao, B., Su, P., Zhu, J., Chen, J., Xu, Y., Gu, B., Liu, Y., Wang, L., 2018. Talanta 190, 204–209.
Chen, S., Chen, X., Zhang, L., Gao, J., Ma, Q., 2017. ACS Appl. Mater. Inter. 9 (6), 5430–5436.
Chinen, A.B., Guan, C.M., Ferrer, J.R., Barnaby, S.N., Merkel, T.J., Mirkin, C.A., 2015. Chem. Rev. 115 (19), 10530–10574.
Chu, M., Kang, J., Wang, W., Li, H., Feng, J., Chu, Z., Zhang, M., Xu, L., Wang, Y., 2015. Cell. Mol. Immunol. 14 (4), 398–400.
Cohen, R.B., 2003. Clin. Colorectal Canc. 2 (4), 246–251.
Crulhas, B.P., Karpik, A.E., Delella, F.K., Castro, G.R., Pedrosa, V.A., 2017. Anal. Bioanal. Chem. 409 (29), 6771–6780.
Díaz, U., Corma, A., 2016. Coord. Chem. Rev. 311, 85–124.
Ding, S., Dong, M., Wang, Y., Chen, Y., Wang, H., Su, C., Wang, W., 2016. J. Am. Chem. Soc. 138 (9), 3031–3037.
Elshafey, R., Tavares, A.C., Siaj, M., Zourob, M., 2013. Biosens. Bioelectron. 50, 143–149.
Emami, M., Shamsipur, M., Saber, R., Irajirad, R., 2014. Analyst 139 (11), 2858–2866.
Gao, Q., Li, X., Ning, G., Leng, K., Tian, B., Liu, C., Tang, W., Xu, H., Loh, K.P., 2018. Chem. Commun. 54 (19), 2349–2352.
Geng, T., Ye, S., Zhu, Z., Zhang, W., 2018. J. Mater. Chem. A 6 (6), 2808–2816.
Guo, Y., Shu, Y., Li, A., Li, B., Pi, J., Cai, J., Cai, H., Gao, Q., 2017. J. Mater. Chem. B 5 (28), 5532–5538.
Hasanzadeh, M., Shadjou, N., de la Guardia, M., 2017. TrAC Trend Anal. Chem. 91, 67–76.
Hashkavayi, A.B., Raoof, J.B., Ojani, R., Kavoosian, S., 2017. Biosens. Bioelectron. 92, 630–637.
He, L., Duan, F., Song, Y., Guo, C., Zhao, H., Tian, J., Zhang, Z., Liu, C., Zhang, X., Wang, P., Du, M., Fang, S., 2017. 2D Mater. 4 (2), 25098.
Hirsch, F.R., Dziadziuszko, R., Thatcher, N., Mann, H., Watkins, C., Parums, D.V., Speake, G., Holloway, B., Bunn, P.A., Franklin, W.A., 2008. Cancer-Am. Cancer Soc. 112 (5), 1114–1121.
Ilkhani, H., Sarparast, M., Noori, A., Zahra Bathaie, S., Mousavi, M.F., 2015. Biosens. Bioelectron. 74, 491–497.
Johari-Ahar, M., Karami, P., Ghanei, M., Afkhami, A., Bagheri, H., 2018. Biosens. Bioelectron. 107, 26–33.
Li, J., Wang, J., Zhang, X., Chang, H., Wei, W., 2018a. Sens. Actuat. B-Chem. 273, 1300–1306.
Li, R., Huang, H., Huang, L., Lin, Z., Guo, L., Qiu, B., Chen, G., 2013. Electrochim. Acta 109, 233–237.
Li, W., Yang, C., Yan, X., 2017. Chem. Commun. 53 (83), 11469–11471.
Li, X., Shen, C., Yang, M., Rasooly, A., 2018b. Anal. Chem. 90 (7), 4764–4769.
Loan, P.T.K., Wu, D., Ye, C., Li, X., Tra, V.T., Wei, Q., Fu, L., Yu, A., Li, L., Lin, C., 2018. Biosens. Bioelectron. 99, 85–91.
Ma, F., Li, Y., Tang, B., Zhang, C., 2016. Acc. Chem. Res. 49 (9), 1722–1730.
Magar, H.S., Ghica, M.E., Abbas, M.N., Brett, C.M.A., 2017. Talanta 167, 462–469.
Meng, H., Liu, H., Kuai, H., Peng, R., Mo, L., Zhang, X., 2016. Chem. Soc. Rev. 45 (9), 2583–2602.
Mousavi, M.F., Mirsian, S., Noori, A., Ilkhani, H., Sarparast, M., Moradi, N., Bathaie, S.Z.,

Mehrgardi, M.A., 2016. Electroanal 29 (3), 861–872.
Nguyen, V., Lee, B.H., Kim, S.H., Gu, M.B., 2016. Biotechnol. J. 11 (6), 843–849.
Omidfar, K., Darzianiazizi, M., Ahmadi, A., Daneshpour, M., Shirazi, H., 2015. Sens. Actuat. B-Chem. 220, 1311–1319.
Pauchard, V., Rane, J.P., Zarkar, S., Couzis, A., Banerjee, S., 2014. Langmuir 30 (28), 8381–8390.
Peng, Y., Huang, Y., Zhu, Y., Chen, B., Wang, L., Lai, Z., Zhang, Z., Zhao, M., Tan, C., Yang, N., Shao, F., Han, Y., Zhang, H., 2017. J. Am. Chem. Soc. 139 (25), 8698–8704.
Pfeiffer, P., Nexø, E., Bentzen, S.M., Clausen, P.P., Andersen, K., Rose, C., 1998. Brit. J. Cancer 78, 96–99.
Qian, H., Dai, C., Yang, C., Yan, X., 2017. ACS Appl. Mater. Inter. 9 (29), 24999–25005.
Razmi, N., Baradaran, B., Hejazi, M., Hasanzadeh, M., Mosafer, J., Mokhtarzadeh, A., de la Guardia, M., 2018. Biosens. Bioelectron. 113, 58–71.
Regiart, M., Fernández-Baldo, M.A., Villarroel-Rocha, J., Messina, G.A., Bertolino, F.A., Sapag, K., Timperman, A.T., Raba, J., 2017. Anal. Chim. Acta 963, 83–92.
Shi, P., Zhang, Y., Yu, Z., Zhang, S., 2017. Sci. Rep. -UK 7, 6500.
Song, Y., Duan, F., Zhang, S., Tian, J., Zhang, Z., Wang, Z., Liu, C., Xu, W., Du, M., 2017. J. Mater. Chem. A 5 (36), 19378–19389.
Suzuki, Y., Endo, M., Sugiyama, H., 2015. Nat. Commun. 6, 8052.
Tan, L., Chen, Z., Zhao, Y., Wei, X., Li, Y., Zhang, C., Wei, X., Hu, X., 2016. Biosens. Bioelectron. 85, 414–421.
Thariat, J., Etienne-Grimaldi, M., Grall, D., Bensadoun, R., Cayre, A., Penault-Llorca, F., Veracini, L., Francoual, M., Formento, J., Dassonville, O., De Raucourt, D., Geoffrois, L., Giraud, P., Racadot, S., Morinière, S., Milano, G., Van Obberghen-Schilling, E., 2012. Clin. Cancer Res. 18 (5), 1313–1322.
Top, M., Er, O., Congur, G., Erdem, A., Lambrecht, F.Y., 2016. Talanta 160, 157–163.
Vasudev, A., Kaushik, A., Bhansali, S., 2013. Biosens. Bioelectron. 39 (1), 300–305.
Vinayan, B.P., Nagar, R., Rajalakshmi, N., Ramaprabhu, S., 2012. Adv. Funct. Mater. 22 (16), 3519–3526.
Wan, S., Gándara, F., Asano, A., Furukawa, H., Saeki, A., Dey, S.K., Liao, L., Ambrogio, M.W., Botros, Y.Y., Duan, X., Seki, S., Stoddart, J.F., Yaghi, O.M., 2011. Chem. Mater. 23 (18), 4094–4097.
Wang, L., Xiong, Q., Xiao, F., Duan, H., 2017a. Biosens. Bioelectron. 89, 136–151.
Wang, P., Kang, M., Sun, S., Liu, Q., Zhang, Z., Fang, S., 2014. Chin. J. Chem. 32 (9), 838–843.
Wang, R., Wang, X., Sun, Y., 2017b. Sens. Actuat. B-Chem. 241, 73–79.
Wang, Y., Ge, S., Zhang, L., Yu, J., Yan, M., Huang, J., 2017c. Biosens. Bioelectron. 89, 859–865.
Xiong, Y., Su, L., He, X., Duan, Z., Zhang, Z., Chen, Z., Xie, W., Zhu, D., Luo, Y., 2017. Sens. Actuat. B-Chem. 253, 384–391.
Yang, J., Dou, B., Yuan, R., Xiang, Y., 2017a. Anal. Chem. 89 (9), 5138–5143.
Yang, X., Lv, J., Yang, Z., Yuan, R., Chai, Y., 2017b. Anal. Chem. 89 (21), 11636–11640.
Zejli, H., Goud, K.Y., Marty, J.L., 2018. Talanta 185, 513–519.
Zhang, D., Ma, F., Zhang, Q., Zhang, C., 2017a. Chem. Commun. 53 (83), 11496–11499.
Zhang, F., Wang, S., Yin, L., Yang, Y., Guan, Y., Wang, W., Xu, H., Tao, N., 2015. Anal. Chem. 87 (19), 9960–9965.
Zhang, T., Chai, H., Meng, F., Guo, Z., Jiang, Y., Miao, P., 2018a. ACS Appl. Mater. Inter. 10 (43), 36796–36804.
Zhang, Y., Guo, S., Huang, H., Mao, G., Ji, X., He, Z., 2018b. Anal. Chim. Acta 1035, 154–160.
Zhang, Z., Ji, H., Song, Y., Zhang, S., Wang, M., Jia, C., Tian, J., He, L., Zhang, X., Liu, C., 2017b. Biosens. Bioelectron. 94, 358–364.